REPORT

CRYSTAL GROWTH

Controlled growth and form of precipitating microsculptures

C. Nadir Kaplan,[1,2]* Wim L. Noorduin,[1,3]* Ling Li,[1,4,5] Roel Sadza,[1] Laura Folkertsma,[1] Joanna Aizenberg,[1,2,4,6] L. Mahadevan[1,2,4,7]†

Controlled self-assembly of three-dimensional shapes holds great potential for fabrication of functional materials. Their practical realization requires a theoretical framework to quantify and guide the dynamic sculpting of the curved structures that often arise in accretive mineralization. Motivated by a variety of bioinspired coprecipitation patterns of carbonate and silica, we develop a geometrical theory for the kinetics of the growth front that leaves behind thin-walled complex structures. Our theory explains the range of previously observed experimental patterns and, in addition, predicts unexplored assembly pathways. This allows us to design a number of functional base shapes of optical microstructures, which we synthesize to demonstrate their light-guiding capabilities. Overall, our framework provides a way to understand and control the growth and form of functional precipitating microsculptures.

Microstructures with complex three-dimensional (3D) shapes emerge as important elements in magnetic, electronic, and optical devices (*1*–*4*). Well-defined highly curved and hollow shapes are increasingly essential for sophisticated microphotonic components, such as optical resonance cavities (*5*–*7*), light directors (*8*), photonic trumpets (*9*), and next-generation optical metamaterials (*4*, *10*, *11*). Currently, none of the existing fabrication approaches takes full advantage of the physicochemical processes that arise in natural systems. Top-down lithographic manufacturing has the capability of creating complex 3D geometries precisely but is laborious and difficult to scale up. Similarly, molding and 3D printing show enormous potential in building intricate shapes but have limited ability to control feature sizes at the submicron scale (*12*, *13*). Finally, droplet microfluidics or colloidal self-assembly are simple and scalable but typically form highly symmetric superstructures (*14*, *15*).

A promising candidate for the bottom-up fabrication of cheap, scalable, and intricate geometries is the biomineralization-inspired coprecipitation of silica with barium or strontium carbonates (*16*–*22*). The resulting structures—such as vases, corals, and helices (Fig. 1, A to D)—can be rationally sculpted by modulating the reaction conditions (*22*). Although semiempirical arguments allow for a qualitative view of the mechanisms involved, the absence of a quantitative theoretical framework makes it difficult to characterize or control these precipitation patterns. Here, we provide a geometrical theory for the morphogenesis of carbonate-silica coprecipitation as an interface growth problem. We use the theory to explore the range of possible shapes and determine ways to control them.

When CO_2 flows into an alkaline aqueous solution (pH = 11 to 12) of barium chloride ($BaCl_2$) and sodium metasilicate (Na_2SiO_3), carbonate-silica structures coprecipitate in three stages (Fig. 1E) [section I. A in the supplementary materials (SM)]: (i) Barium carbonate ($BaCO_3$) crystallizes in the entire basic pH range according to $Ba^{2+} + CO_2 + H_2O \rightarrow BaCO_3\,(s) + 2H^+$ (Fig. 1F); (ii) the local decrease in the pH triggers the acid-catalyzed reaction of silicate to orthosilicic acid [$Si(OH)_4$] in a narrow pH range (Fig. 1F and Eq. S2) and its polycondensation into amorphous SiO_2 on the dendritic $BaCO_3$ crystals (*23*), leading to cylindrical posts; and (iii) abundant CO_2 dissolved in the solution induces splitting of the growing tips into either a single connected front at high nucleation densities or multiple disconnected fronts at low nucleation densities, both of which form thin walls composed of rod-shaped $BaCO_3$ nanocrystals coated by SiO_2 on the lateral wall faces (section II. A in the SM) (*20*, *22*). Because $BaCO_3$ is produced at higher rates than SiO_2 (section II. A in the SM), the pH at the growth site is lower than that in the bulk solution. Note that when the local pH is within the SiO_2 deposition range, silica precipitates and terminates the growth of $BaCO_3$ crystals. Therefore, successful carbonate-silica coprecipitation only occurs when the local pH at the growth front is either slightly above (regime I) or below (regime II) the SiO_2 deposition range, so as to sustain continuous carbonate precipitation (*22*) (Fig. 1F; section II. A in the SM).

In regime I, the pH of the solution is set significantly higher (pH ≈ 12) than that associated with SiO_2 deposition, resulting in growth directed from the low-pH front toward the high-pH bulk solution where the $BaCO_3$ supersaturation is higher (Fig. 1F). Consequently, at high nucleation densities, vaselike (Fig. 1A) and petal-like (Fig. 1B) structures grow steeply away from the vicinity of other growing fronts, whereas at low nucleation densities, multiple fronts originating from a single root blossom into coral-like structures (Fig. 1C). We quantified the growth in this regime via a microfluidic reactor that allowed for direct in situ visualization under constant reaction conditions (section I. B to D in the SM and movie S1). When CO_2 enters the microfluidic channel through a membrane, corals nucleate in distinct bands (Fig. 1G) with a spatial and temporal periodicity (section I. E in the SM). Approximating each coral by a hemisphere with a time-dependent radius $R(t)$, we find that the projected circular area of the corals grows linearly in time ($\pi R^2 \cong t$) with a rate of 30 to 50 μm^2/min (Fig. 1H). The radius R and the growth speed, U, scale as $R \cong \sqrt{t}$ and $U \equiv dR/dt \cong 1/R$, respectively, i.e., growth is diffusion-controlled at the coprecipitation fronts with a rate proportional to the interfacial curvature, $1/R$ (*24*, *25*). In the vicinity of the front, the soluble silica oligomers may buffer the local acidity and act as slow-diffusing species. The growth of corals reduces the local pH and eventually stops when silica passivates the low-pH fronts that approach each other.

In regime II, the initial bulk solution pH only slightly exceeds that for silica deposition (pH ≈ 11). Carbonate precipitation steers the structures toward each other's growth fronts or close to the substrate, where the local pH at the growth site remains below the pH range of excessive silica formation that would overgrow $BaCO_3$ crystals and passivate growth (*22*) (Fig. 1F). This yields helical or leaf-shaped structures (fig. S6C), which develop a high-curvature front that must result in a lower oligomer concentration at the interface (*25*). The buffering ability of the oligomers is then reduced, which induces the lowering of the local pH. As a result, structures inherently bend away from the bulk with an increased curvature. Helical structures display a high edge-to-surface ratio with strong curling of the walls, both of which reduce the pH at the growth site (Fig. 1D). Leaves grow along the substrate by forming a curved front (fig. S6C), which must again sustain carbonate precipitation by having a localized zone of sufficiently low pH at the growth site. Evolving leaves develop tips with high curvature, where the precipitation rate increases and, in turn, sharpens the tips even more (*21*). We interpret this as a growth instability characteristic of a diffusion-limited process (*25*).

In either regime, after front splitting [Fig. 1E, stage (iii)], a diffusion-limited growth front lays down a thin-walled structure. The wall thickness, w, is limited by the SiO_2 precipitation to $w \approx 0.5$ to 0.8 μm even as the wall itself continues to

[1]Paulson School of Engineering and Applied Sciences, Harvard University, Cambridge, MA 02138, USA. [2]Kavli Institute for Bionano Science and Technology, Harvard University, Cambridge, MA 02138, USA. [3]AMOLF, 1098 XG Amsterdam, Netherlands. [4]Wyss Institute for Biologically Inspired Engineering, Cambridge, MA 02138, USA. [5]Department of Mechanical Engineering, Virginia Tech, Blacksburg, VA 24061, USA. [6]Department of Chemistry and Chemical Biology, Harvard University, Cambridge, MA 02138, USA. [7]Department of Physics, Harvard University, Cambridge, MA 02138, USA.
*These authors contributed equally to this work. †Corresponding author. Email: lmahadev@g.harvard.edu

extend laterally over lengths of order 10 μm or larger (section II. A in the SM). The resulting low-aspect ratio structure may thus be well approximated as a surface that is left behind by a space curve, which represents the growth front and evolves over time (Fig. 2A). The instantaneous configuration of the growth front and its embedding in the surface can be formulated in terms of the curve metric, g; the geodesic curvature, κ_g; the normal curvature, κ_N; the geodesic torsion, τ_g; and the second normal curvature, $\kappa_{N,2}$ (Fig. 2, B and C, and table S2). The variables κ_g, κ_N, τ_g, and g are linked by the partial differential equations of surface theory in differential geometry (*26*) that embody the geometric constraints on the curve embedded in a surface (section II. B in the SM). The position of the moving front $\vec{\mathbf{X}}$ is determined by its evolving Lagrangian velocity

$$\frac{d\vec{\mathbf{X}}}{dt} = \hat{\mathbf{n}}U \qquad (1)$$

where $\hat{\mathbf{n}}$ is the growth direction, U is the local speed of the curved front, $d/dt \equiv \partial/\partial t|_{\vec{\mathbf{X}}(s,t)}$ (see Fig. 2A). To characterize the diffusion-limited accretion, we assume that U is a function of the local geometry of the growth front, as in dendritic patterning processes (*27*). Our assumption is justified by the localized growth due to the coprecipitation reactions (Eqs. S1 and S2) and slow diffusion of soluble silica oligomers. This corresponds to the inequality $w \ll L_D < L_\kappa$, where w is the wall thickness, L_D is the diffusion length and L_κ is the radius of curvature. In contrast, growth of a 2D front in dendritic solidification is diffusion-controlled only when it is nonlocal, i.e., $L_D > L_\kappa$ (section II. C in the SM). Writing $U = U(\kappa_g, \kappa_N, \tau_g, \kappa_{N,2})$ and expanding this function as a power series up to cubic order (section II. D in the SM), the resulting equations of motion for U and the geometrical variables (g, κ_g, κ_N, τ_g, $\kappa_{N,2}$) yield the position of the growth front $\vec{\mathbf{X}}$ from Eq. 1, and the surface left behind by it, given the second normal curvature, $\kappa_{N,2}$.

The variable $\kappa_{N,2}$ controls the local bend distortions along the growth direction, $\hat{\mathbf{n}}$, and it is either enhanced or reduced by the initial pH of the bulk solution. This suggests a pH-dependent coarse-grained bending parameter $q_b = q_b(\mathrm{pH})$. In regime I, the growth direction toward the high-pH solution is roughly preserved (Fig. 1, A and B); thus, q_b must be low. In regime II, inward-directed growth toward lower pH forces the structures to curl gradually at the interface (Fig. 1D); therefore, q_b must be high. Experimentally, the bending deformations are governed by the pH gradients at the scale of the wall thickness, w (Fig. 2A). Because we focus on the wall morphogenesis at length scales much bigger than w, we propose the following phenomenological equation of motion for $\kappa_{N,2}$ to characterize both regimes

$$\frac{d\kappa_{N,2}}{dt} = \gamma\frac{\partial^2\kappa_{N,2}}{\partial s^2} + \zeta\kappa_g\kappa_N U(\kappa_{N,2} - q_b) \qquad (2)$$

The first term on the right models the diffusive relaxation of the curling mode along the edge (*20*) with a diffusivity γ (Fig. 2D). The second term controls bending with a rate ζ by accounting for the following observations: First, bending saturates when $\kappa_{N,2} = q_b$; second, the sign of the geodesic curvature, κ_g, determines whether bending should increase or decrease, which allows for dynamic modulations between different growth regimes; third, bending increases more slowly in relatively flat sections with a small normal curvature, κ_N, than in already curled regions with a higher κ_N; and last, bending stops when the speed U vanishes. Eqs. 1 and 2, and the geometrical compatibility relations (section II. B in the SM), complete the formulation of the problem when initial and boundary conditions are provided.

Given q_b and the angle β that sets the initial orientation of $\hat{\mathbf{n}}$, we simulated the evolution of walls that emerge after front splitting [Fig. 1E, stage (iii)], in particular the vaselike and petal-like structures in regime I and helices in regime II (section II. E in the SM and movies S2 to S6). In Fig. 3A, we show the formation of vases that start from a circle of radius ℓ. To model the experimentally observed correlation between the high nucleation density of precipitates and vase formation, we take the initial growth direction to be strongly out of the substrate plane (β: large, Fig. 1E). As the planar and circular growth site of a vase expands over time, its geodesic curvature, κ_g, decreases (Fig. 2B). When the growth speed U is linear in κ_g, we analytically deduce that the projected area of a vase varies linearly in time (section II. F in the SM). By contrast, growth is sublinear when U also depends on higher-order terms (fig. S8), and the projected area of a vase as a function of time is in accordance with the microfluidics experiments at low q_b (Fig. 1H). Whereas low values of q_b (high pH) lead to cones, for higher q_b (lower pH) the conical vases start to curve

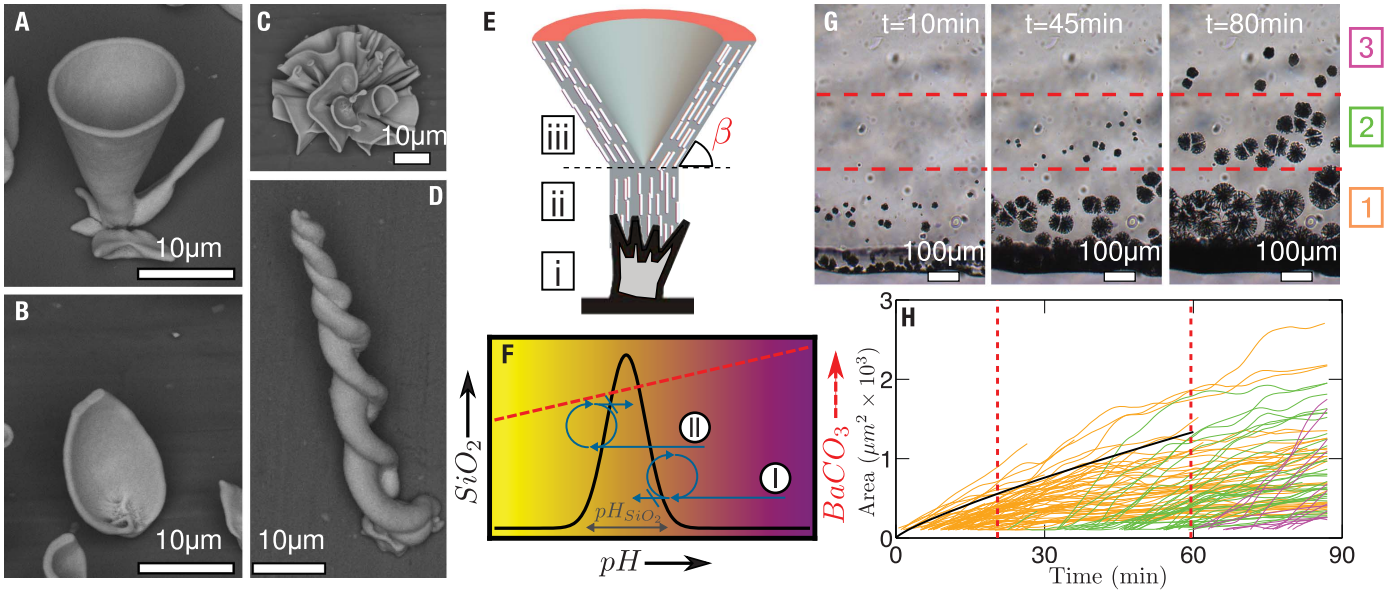

Fig. 1. Carbonate-silica coprecipitation patterns. (**A**) to (**D**) Scanning electron microscopy (SEM) images of the typical (A) vaselike, (B) petal-like, (C) coral-like, and (D) helical microstructures. (**E**) Stages of coprecipitation: (i) nucleation of the seed carbonate crystal; (ii) outgrowth of carbonate/silica coprecipitate; (iii) splitting of the thin wall. The initial slope between a thin wall and the substrate is defined by β. (**F**) Schematics of the SiO_2 (solid black curve) and $BaCO_3$ (dashed red line) precipitation rates between pH 8 and 12 (*22*). Regimes I and II are indicated. (**G**) Growth of coral-like structures produces three distinct bands (marked alongside with orange, 1; green, 2; and magenta, 3, from bottom to top) in a microfluidic chamber where the CO_2 flows from the bottom edge. (**H**) Projected circular area of growing corals as a function of time [line colors correspond to the bands in (G)], and the simulated growth of a conical vase for the bending parameter $q_b = 10^{-3}$ (black line, see text).

inwards (Fig. 3A). When the speed of the front is set to zero at a point of the advancing front that starts from a circle, we see nonuniform growth associated with the local passivation by silica overcoating. This leads to the formation of petals for both low and high q_b as shown in Fig. 3B and fig. S9, respectively, and in agreement with experiments (Fig. 1B).

Finally, helices emerge by means of the unstable growth of a nearly semicircular front as shown in Fig. 3C. We observe that the pitch and overall size of the helices become larger when q_b decreases (fig. S10), whereas the growth reaches a steady state at lower q_b with a constant pitch and width over the twisted region. At still higher q_b, the helices develop tips and stop (fig. S10), consistent with experiments (*20*, *22*). For an areal growth rate of 40 μm²/min and an initial radius of $\ell \sim 2$ μm, we see that vases and helices reach a size of $\mathcal{O}$(10 μm) in $\mathcal{O}$(10 min), in quantitative agreement with experiments (fig. S8) (see section III. A in the SM for the stereolithography files of the simulated sculptures).

Our theoretical framework couples two physicochemical processes to the instantaneous local geometry of the reaction front and, in turn, the morphology of carbonate-silica precipitates. These processes are the diffusion-limited growth, which is localized by the condition $L_D < L_\kappa$ (where L_D is the diffusion length and L_κ, local radius of curvature) and, hence, quantified by the local growth rate U, and the effect of solution pH on the emergence of curling deformations, modeled by the bending parameter q_b and Eq. 2. The agreement between theoretical and experimental shapes establishes the relation between q_b and pH, as plotted in Fig. 3D.

Photonic microcomponents—such as optical waveguides, light directors (*8*), and Bragg resonators (*7*)—are excellent candidates for bottom-up design owing to their shell-like geometries and stringent tolerances. Given the transparency and relatively high refractive index n of the carbonate salts (n = 1.5 to 1.7) and silica (n = 1.5), the similarity of size and shape between vaselike precipitates (Fig. 3A) and top-down lithographically fabricated analogs (*8*, *9*) suggests the use of our bottom-up strategy to build optical components. To solve the inverse problem of designing functional shapes, we split the simulations into a sequence of steps corresponding to switching growth

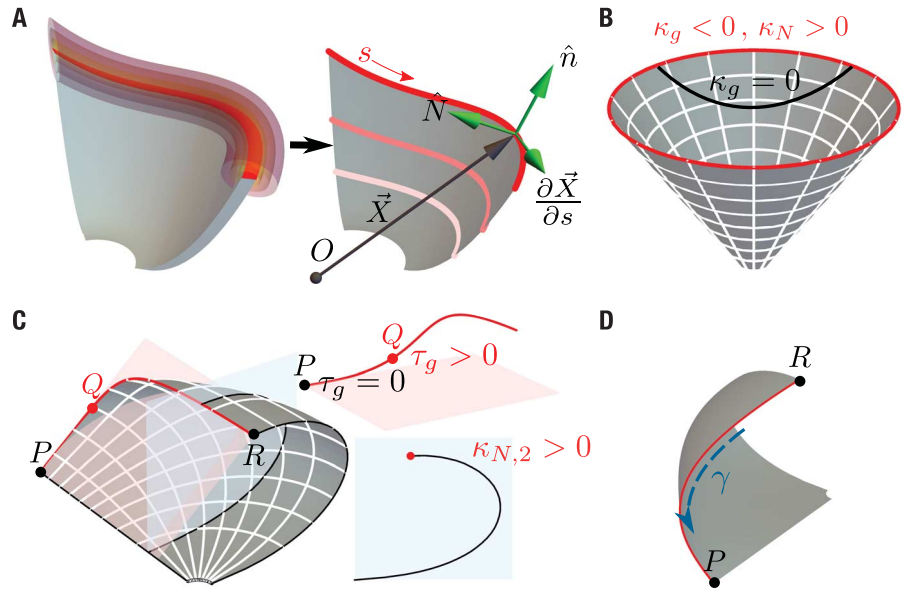

Fig. 2. Geometry of growth. (**A**) Precipitation in a narrow semicylindrical edge zone leaves behind a thin wall (left). Colors depict the pH values (Fig. 1F). We represent the moving growth front as a curve (shades of red, right) with a position vector, $\vec{\mathbf{X}}(s,t)$. An orthonormal triad is formed by the curve tangent, $\partial\vec{\mathbf{X}}/\partial s$, the growth direction $\hat{\mathbf{n}}$, both of which lie in the surface, and the surface normal, $\hat{\mathbf{N}} \equiv \partial\vec{\mathbf{X}}/\partial s \times \hat{\mathbf{n}}$. (**B**) The front geometry is partly determined by the geodesic curvature, κ_g, the curvature of a line with respect to a geodesic (κ_g = 0) on a surface (*26*). Folding a plane into the cone introduces a normal curvature (κ_N) along the curve. (**C**) Unless the orthonormal triad twists, the geodesic torsion, τ_g, characterizes a nonplanar curve; it is zero around the point P where the front is tangent to the light red plane. At point Q, the front becomes a space curve (as τ_g is finite). The second normal curvature, $\kappa_{N,2}$, is associated with the bending of the surface at the front (black curve on the light blue plane). (**D**) Curling diffuses from high $\kappa_{N,2}$ (at R) to lower $\kappa_{N,2}$ (around P) with diffusivity γ according to Eq. 2.

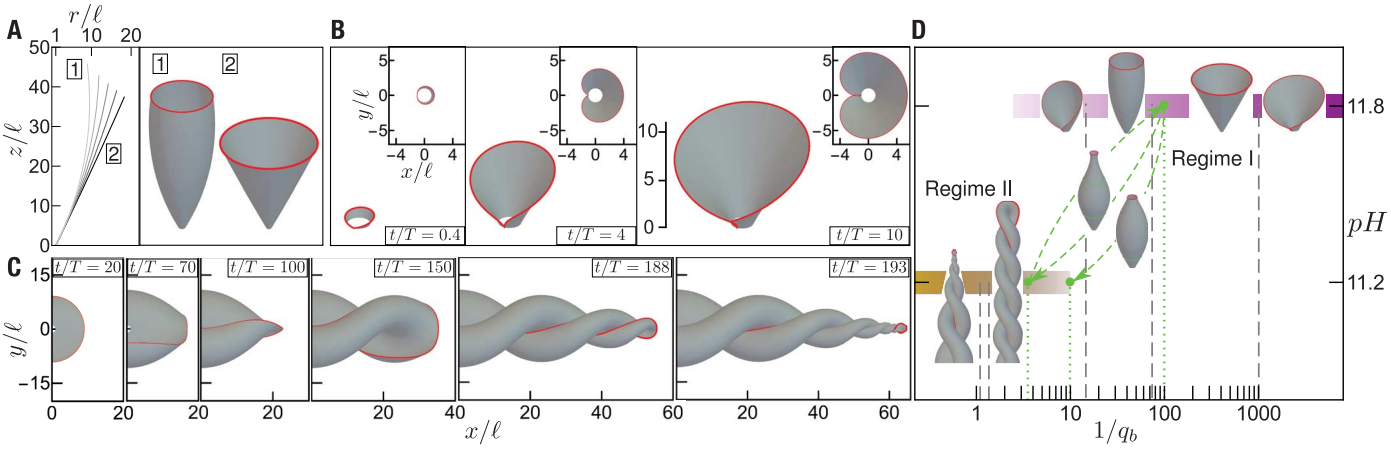

Fig. 3. Dynamics of form. (**A**) (Left) Axisymmetric profiles of the vases as a function of the bending parameter $q_b \in [10^{-3} - 0.013]$ in 3 × 10^{-3} increments with the gray scale changing from dark to light. (Right) Resulting vases corresponding to q_b = 0.013 (1) and $q_b = 10^{-3}$ (2). (**B**) Time evolution of petal growth ($q_b = 10^{-3}$), showing the elevated and plan views. (**C**) Growth of a helical precipitate (q_b = 0.9). In (A) to (C), the lengths x, y, z, and r are scaled by ℓ, defined as the radius of the initial circular front, and the time is scaled by T (see section II. E in the SM). (**D**) Relation between the reciprocal bending parameter $1/q_b$ and the initial solution pH (regime I pH, magenta; regime II pH, orange) defines the two regimes. The q_b value of each structure is represented by the nearest dashed gray line. The structures grown by the successive modulations between the two regimes (green dashed arrows) correspond to a set of q_b values (green dotted lines) (Fig. 4A).

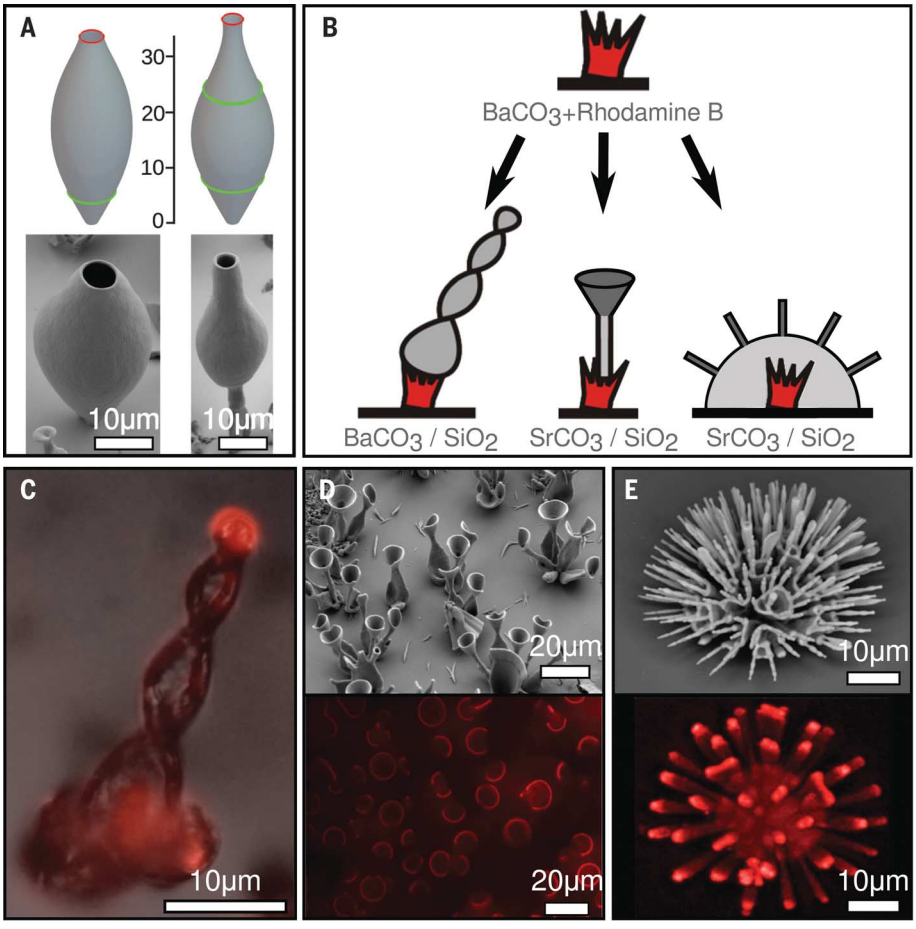

Fig. 4. Controlled growth and form of optical microcomponents. (**A**) Simulations (top) and experimental realization (bottom) of the base shapes for Bragg resonators. The simulations correspond to the sequences q_b = 0.01, 0.1 (top, left) and q_b = 0.01, 0.3, 0.01 (top, right). The green curves denote the heights at which q_b changes. The lengths are scaled by ℓ. Likewise, the experimental shapes are grown by two (bottom, left) and three (bottom, right) steps. (**B**) Schematics for synthesizing microstructures with integrated light source (red) and waveguide properties. The gray scale denotes the growth sequence (section I. G in the SM). (**C**) Helical structure (overlay of fluorescence and optical microscopy) and (**D**) trumpet-shaped assemblages (top, SEM image, and bottom, confocal microscopy image) that operate as waveguides. (**E**) A coral decorated with posts (top, SEM) acting as a beamsplitter (bottom, confocal).

conditions from regime I to regime II, where the final state of the growth site from the preceding step serves as the initial condition for the next regime (movies S7 and S8). For example, our theory predicts that curved precipitates depicted in Fig. 4A (top) may arise in two or three consecutive steps. Starting from a vase with low q_b (high pH), inducing bend at a higher q_b (lower pH) results in the formation of hollow shapes that resemble spherically symmetrical Bragg resonators (*5*, *6*). Reverting to a low q_b (high pH) as a third step plants a narrow neck on top and generates the base shape of an onionlike Bragg resonator similar to that described in (*7*). This theoretical sequence of alternating growth conditions associated with stepwise changes of q_b in the model corresponds to the control of the pH around a structure (Fig. 3D), indicating how these geometries can also be realized experimentally. These shapes were successfully synthesized following the theoretical guidance (Fig. 4A, bottom, and section I. F in the SM).

To demonstrate that our carbonate-silica precipitates are optically functional, we incorporated a light source in the system. Crystallizing $BaCO_3$ can be doped with organic additives, including dyes, during precipitation (*28*). To this end, for the growth stage (i), we introduced the fluorescent dye rhodamine B into the initial solution containing $BaCl_2$ (section I. G in the SM). The resulting $BaCO_3$ crystals with the embedded light source served as seeds for subsequent dye-free synthesis of various $BaCO_3$-SiO_2 or $SrCO_3$-SiO_2 microstructures at the growth stages (ii) and (iii) (Fig. 4B), in which light is effectively directed from the fluorescent crystal to the edge. The thus synthesized helix, photonic trumpets, and an array of posts grown atop a coral, which clearly demonstrate the ability to guide or split light beams, are shown in Fig. 4, C to E.

Our theoretical model explains the range of patterns in a carbonate-silica system and offers a means to guide the synthesis of complex 3D shapes. We have used this bottom-up strategy to make functional optical microarchitectures using the underlying physicochemical processes in sharp contrast to top-down lithographic methods. When combined with an optimization algorithm for process control, our approach has the potential to provide a scalable, inexpensive, and accurate strategy to create 3D photonic microstructures.

REFERENCES AND NOTES

1. S. Xu *et al.*, *Science* **347**, 154–159 (2015).
2. P. X. Gao *et al.*, *Science* **309**, 1700–1704 (2005).
3. B. M. Ross, L. Y. Wu, L. P. Lee, *Nano Lett.* **11**, 2590–2595 (2011).
4. M. Decker, M. W. Klein, M. Wegener, S. Linden, *Opt. Lett.* **32**, 856–858 (2007).
5. M. A. Kaliteevski, S. Brand, R. A. Abram, V. V. Nikolaev, *J. Mod. Opt.* **48**, 1503–1516 (2001).
6. D. Brady, G. Papen, J. E. Sipe, *J. Opt. Soc. Am. B* **10**, 644 (1993).
7. Y. Xu, W. Liang, A. Yariv, J. G. Fleming, S.-Y. Lin, *Opt. Lett.* **29**, 424–426 (2004).
8. J. H. Atwater *et al.*, *Appl. Phys. Lett.* **99**, 151113 (2011).
9. M. Munsch *et al.*, *Phys. Rev. Lett.* **110**, 177402 (2013).
10. C. M. Soukoulis, S. Linden, M. Wegener, *Science* **315**, 47–49 (2007).
11. J. K. Gansel *et al.*, *Science* **325**, 1513–1515 (2009).
12. J. L. Perry, K. P. Herlihy, M. E. Napier, J. M. Desimone, *Acc. Chem. Res.* **44**, 990–998 (2011).
13. J. R. Tumbleston *et al.*, *Science* **347**, 1349–1352 (2015).
14. S. S. Datta *et al.*, *Adv. Mater.* **26**, 2205–2218 (2014).
15. X. Ye *et al.*, *Proc. Natl. Acad. Sci. U.S.A.* **107**, 22430–22435 (2010).
16. L. A. Gower, D. A. Tirrell, *J. Cryst. Growth* **191**, 153–160 (1998).
17. A. G. Shtukenberg, Y. O. Punin, A. Gujral, B. Kahr, *Angew. Chem. Int. Ed. Engl.* **53**, 672–699 (2014).
18. Y.-Y. Kim *et al.*, *Nat. Mater.* **15**, 903–910 (2016).
19. J. M. García-Ruiz *et al.*, *Science* **302**, 1194–1197 (2003).
20. J. M. García-Ruiz, E. Melero-García, S. T. Hyde, *Science* **323**, 362–365 (2009).
21. M. Kellermeier *et al.*, *Chemistry* **18**, 2272–2282 (2012).
22. W. L. Noorduin, A. Grinthal, L. Mahadevan, J. Aizenberg, *Science* **340**, 832–837 (2013).
23. D. J. Belton, O. Deschaume, C. C. Perry, *FEBS J.* **279**, 1710–1720 (2012).
24. N. Goldenfeld, *J. Cryst. Growth* **84**, 601–608 (1987).
25. J. S. Langer, *Rev. Mod. Phys.* **52**, 1–28 (1980).
26. J. J. Stoker, *Differential Geometry* (Wiley, New York, 1969).
27. R. C. Brower, D. A. Kessler, J. Koplik, H. Levine, *Phys. Rev. Lett.* **51**, 1111–1114 (1983).
28. B. Kahr, R. W. Gurney, *Chem. Rev.* **101**, 893–951 (2001).

ACKNOWLEDGMENTS

The authors thank J. A. Fritz, M. Kolle, M. Lončar, and T. M. Schneider for fruitful discussions and P. A. Korevaar, W. M. van Rees, J. C. Weaver, and T. C. Ferrante for technical assistance. This research was supported by NSF Designing Materials to Revolutionize and Engineer Our Future under award 15-33985, the Kavli Institute for Bionano Science and Technology at Harvard University, and the Harvard MRSEC under award 14-20570. W.L.N. thanks the Netherlands Organization for Scientific Research (NWO) for financial support from a VENI grant. R.S. acknowledges Technical University Eindhoven's Fonds Ectspunten Buitenland financial support, and L.F. the Radboud University Nijmegen study fund. L. M. was partially supported by fellowships from the MacArthur Foundation and the Radcliffe Institute. Scanning and transmission electron microscopies were performed at the Center for Nanoscale Systems at Harvard University, supported by the NSF under award ECS-0335765, and the Amsterdam nanoCenter, supported by NWO. The authors declare no conflicts of interest.

SUPPLEMENTARY MATERIALS

www.sciencemag.org/content/355/6332/1395/suppl/DC1
Materials and Methods
Supplementary Text
Figs. S1 to S10
Tables S1 to S3
Movie Legends S1 to S8
Database Legends S1 to S11
References (*29*–*31*)
Movies S1 to S8
Data Files S1 to S11

24 July 2016; resubmitted 31 October 2016
Accepted 9 March 2017
10.1126/science.aah6350

Editor's Summary

Predicting the shape of crystals to come

Coprecipitating carbonate and silica can form complex three-dimensional shapes. These range from flowers to trumpets, depending on the pH. Kaplan *et al.* developed a theoretical model to interpret the crystal growth shapes. The model predicts crystal growth shapes under varying experimental conditions and captures the geometrical aspects of morphological development.

Science, this issue p. 1395